Environmental Pollution 256 (2020) 113417

Contents lists available at ScienceDirect

Environmental Pollution

journal homepage: www.elsevier.com/locate/envpol

Porous tube-like ZnS derived from rod-like ZIF-L for photocatalytic Cr(VI) reduction and organic pollutants degradation☆

Yu-Xuan Li [a], Huifen Fu [a], Peng Wang [a], Chen Zhao [a], Wen Liu [b], Chong-Chen Wang [a, *]

[a] Beijing Key Laboratory of Functional Materials for Building Structure and Environment Remediation/Beijing Advanced Innovation Centre for Future Urban Design, Beijing University of Civil Engineering and Architecture, Beijing, 100044, China

[b] The Key Laboratory of Water and Sediment Sciences, Ministry of Education, College of Environment Sciences and Engineering, Peking University, Beijing, 100871, China

ARTICLE INFO

Article history:
Received 18 May 2019
Received in revised form
13 September 2019
Accepted 14 October 2019
Available online 17 October 2019

Keywords:
Metal organic framework
ZnS
Hexavalent chromium
Organic pollutants
Photocatalysis

ABSTRACT

A facile method was developed to fabricate porous tube-like ZnS by sulfurizing rod-like ZIF-L with thioacetamide (TAA) at different durations and the formation mechanism of the porous tube-like ZnS was discussed in detail. The series of sulfide products (ZS-X) were characterized by powder X-ray diffraction (PXRD), Fourier transform infrared spectroscopy (FTIR), solid-state nuclear magnetic resonance spectroscopy (SSNMR), transmission electron microscopy (TEM), UV–visible diffuse-reflectance spectroscopy (UV–vis DRS). The photocatalytic performances of ZS-X toward Cr(VI) reduction and organic pollutant degradation were explored. It was discovered that ZS-3 (porous tube-like ZnS) exhibited excellent activities under UV light and displayed good reusability and stability after several experimental cycles. In addition, Cr(VI) reduction and organic pollutant degradation were investigated under different pH values and existence of different foreign ions. The photocatalytic activities of ZS-3 were tested toward the matrix of Cr(VI) and reactive red X–3B. The mechanism was proposed and verified by both electrochemical analysis and electron spin resonance (ESR) measurement.

1. Introduction

Nowadays, the rapid development of industry is often accompanied by the production of wastewater containing heavy metal ions and organic pollutants. Among the heavy metal ions and organic pollutants, hexavalent chromium (Cr(VI)) and organic dyes are generally highly toxic, harmful to the humans and difficult to be directly carried out biological treatment (Adeyemo et al., 2012; Rengaraj et al., 2007; Wang et al., 2016a; Wang et al., 2014). Cr(VI) is mainly generated from electroplating, textile, leather and other industries, which was presented at a wide range of concentrations, ranging from 0.5 to 270.0 mg L^{-1} in natural surface and groundwater and wastewater (Demirbas et al., 2004; Patterson, 1985). The presence of Cr(VI) in the water environment will increase the human's health risk of liver, kidney and skin cancer (Costa, 1997; Gu et al., 2013; Jing et al., 2005). As well, the organic dyes are chemically stable, and their absorption and reflection of sunlight will further interfere with bacterial growth in the water (Schrank et al., 2002; Wang et al., 2014). Therefore, it is necessary to remove Cr(VI) and organic dyes from wastewater.

Unlike other heavy metals like lead or cadmium, the chromium mainly presents in the form of low-toxic Cr(III) and high-toxic Cr(VI) (Zhang et al., 2014). Some typical methods like precipitation, adsorption and ion exchange were generally adopted to achieve Cr(VI) reduction (Galán et al., 2005; Gheju and Balcu, 2011; Karthikeyan et al., 2005; Kongsricharoern and Polprasert, 1996; Selvi et al., 2001). Photocatalytic conversion of highly toxic Cr(VI) to lowly toxic Cr(III) is considered as one of the most effective strategy because Cr(III) can easily be removed as a solid precipitate like $Cr(OH)_3$ (Khalil et al., 1998; Liang et al., 2015; Rengaraj et al., 2007). For organic dye degradation, photocatalytic reaction makes the dye to be decomposed into biodegradable molecules or low toxic substances, and even completely mineralized into CO_2 and H_2O (Konstantinou and Albanis, 2004; Rauf and Ashraf, 2009).

As a typical wide bandgap semiconductor, ZnS has been used to conduct photocatalytic treatment toward wastewater, due to that it is difficult to be oxidized and hydrolyzed, easily produced with high yield as well as nontoxic (Devulapalli et al., 2015; Fang et al., 2011; Hörner et al., 2015; Jin-Song et al., 2010; Yanagida et al., 1995).

☆ This paper has been recommended for acceptance by Baoshan Xing.

* Corresponding author.
E-mail address: wangchongchen@bucea.edu.cn (C.-C. Wang).

https://doi.org/10.1016/j.envpol.2019.113417
0269-7491/

Nano-scale ZnS materials with different morphologies exhibit good photocatalytic performances in several fields like H_2 evolution (Lee et al., 2016), CO_2 reduction (Eggins et al., 1998; Eggins et al., 1993; Guzman and Martin, 2008, 2009, 2010; Johne and Kisch, 1997; Kanemoto et al., 1992; Zhang and Martin, 2006; Zhou and Guzman, 2014, 2016), organic pollutants degradation (Chao et al., 2010) and Cr(VI) reduction (Hernández-Gordillo et al., 2015). Up to now, various syntheses methods like thermal decomposition (Jin-Song et al., 2010), solvothermal method (Li et al., 2004), thermal evaporation method (Tandra et al., 2009; Wang et al., 2002), and chemical method (Henglein et al., 1984; Tandra et al., 2009) were used to produce ZnS nanostructure with different morphologies like nanowires or nanorods, which required either high temperature or high pressure or both of them. Therefore, in order to meet the practical requirement, it is necessary to explore a facile approach to prepare ZnS with both novel structure and highly photocatalytic activity.

Recently, MOFs (mental-organic frameworks) have attracted extensive attentions due to the large surface areas, intrinsically porous structures and tunable topologies (Qi-Long and Qiang, 2014). The potential applications of MOF have been widely explored in photocatalysis (Seo et al., 2000; Shen et al., 2013; Shen et al., 2015; Wang et al., 2016a; Wang et al., 2014), adsorption (Du et al., 2017; Li et al., 2017), sensing (Hao et al., 2013; Xi et al., 2013) and so on (Rieter et al., 2008; Youn-Sang et al., 2010). Especially, the porous materials derived from MOFs as the precursor have arose considerable interest in many applications including photocatalytic hydrogen generation (Lan et al., 2017), gas sensor (Drobek et al., 2016) and electrocatalysis (Zhou et al., 2017), because the originally structural characteristics of MOF are retained to obtain pore structures with large specific surface area and more active sites (Lan et al., 2017; Wee et al., 2014).

Rod-like ZIF-L is a one-dimensional (1D) MOF constructed from 2-methylimidazole (2-MIM) and Zn^{2+} with the aid of polyvinylpyrrolidone (PVP). It was firstly prepared by Fu et al. in our research group (Fu et al., 2018b) and further used to fabricate porous hollow ZnO as efficient sensor toward acetone (Fu et al., 2018a; Fu et al., 2018b). Inspired by our previous work, within this paper, porous hollow ZnS was harvested from rod-like ZIF-L via sulfidation, which was used to conduct photocatalytic Cr(VI) reduction and organic dyes degradation (Scheme. S1). It is found that the porous tube-like ZnS with good reusability exhibited better photocatalytic performances toward Cr(VI) reduction and dye degradation than P_{25} (commercial TiO_2) and ZnS (Chao et al., 2010; Hernández-Gordillo et al., 2015). Finally, the photocatalytic mechanism was proposed and tested.

2. Experimental

The used materials, the characterization instruments and methods were listed in electronic supplementary information (ESI).

2.1. Preparation of rod-like ZIF-L

Rod-like ZIF-L was prepared by the reported method in the previous literature (Fu et al., 2018b). Briefly, 2.5 g PVP and 8.2 g 2-methylimidazole (2-MIM) were dissolved in 450 mL deionized water. 3.0 g $Zn(NO_3)_2 \cdot 6H_2O$ was dissolved in 50 mL deionized water. Then the two aqueous solutions were mixed under stirring. After stirring evenly and left to stand for 24 h, rod-like ZIF-L was separated by centrifugation, then washed with anhydrous ethanol and finally dried in an oven at 60 °C.

2.2. Preparation of porous tube-like ZnS

The rod-like ZIF-L was sulfurized by thioacetamide (TAA) to produce porous tube-like ZnS. 0.8 g TAA was dissolved in conical flask containing 62 mL ethanol and 40 mL water. The prepared rod-like ZIF-L (0.1 g) was added into the above solution and put in a temperature-controlled shaker (30 °C, 160 r min^{-1}) without further pH adjustment for 1 h, 2 h, 3 h, 6 h, respectively. The target products were obtained via centrifugation, washed three times with anhydrous ethanol, and dried in an oven at 60 °C.

2.3. Photocatalytic test

Considering ZS-3's ability to remove Cr(VI) and previous studies (Babel and Kurniawan, 2004; Liang et al., 2015a), the photocatalytic Cr(VI) reduction experiment was carried out at a concentration of 20 mg L^{-1}, which falls into the concentration range of 0.5–270.0 mg L^{-1} in natural surface and groundwater and wastewater (Demirbas et al., 2004). 40.0 mg as-synthesized ZnS photocatalyst was added into 200 mL Cr(VI) aqueous solution (20 mg L^{-1}) in a quartz reactor. The pH values of the aqueous solutions were adjusted from 4.0 to 10.0 with H_2SO_4 and NaOH solutions, respectively. The suspensions were stirred for 60 min to reach adsorption-desorption equilibrium and then irradiated under UV light with a 500 W Hg lamp (Beijing Aulight Co. Ltd). The 2.0 mL aliquots were extracted every 5.0 min for determination. After being filtered by 0.22 μm PTFE filter, the Cr(VI) concentration was determined by diphenylcarbazide (DPC) method on AutoAnalyzer 3 flow injection Analyzer (Zhong Tong Technical Co. Ltd).

The organic dyes like reactive red X–3B (X–3B, 50 mg L^{-1}), methyl orange (MO, 10 mg L^{-1}), rhodamine B (RhB, 10 mg L^{-1}) and methylene blue (MB, 10 mg L^{-1}) were selected as models to evaluate photocatalytic degradation performance toward organic pollutants of ZnS under UV light, in which the residual dye concentration was tested at the maximum absorbance of 537, 554, 463 and 664 nm for X–3B, RhB, MO and MB with a Laspec Alpha-1860 spectrometer.

The apparent quantum efficiency (AQE) was measured by calculating the removal amount of pollutants under different monochromatic lights, using 300 W Xe lamp (Beijing Aulight Co. Ltd) with different filters. The intensity of the incident light was measured by a CEL-NP2000-2 optical power meter. The AQE calculations of Cr(VI) reduction and X–3B dye degradation followed Equation (1) (Sabate et al., 1992; Velegraki et al., 2018) and Equation (2) (Ao et al., 2008; Sadik, 2007), respectively.

$$AQE\ (Cr) = \frac{3 \times [number\ of\ reduced\ Cr(VI)]}{number\ of\ incident\ photons} \quad (1)$$

$$AQE\ (X-3B) = \frac{rate\ of\ degradation\ molecules\ of\ X-3B}{rate\ of\ incident\ photons\ inside\ reactor} \quad (2)$$

2.4. Electrochemical tests

Electrochemical tests were conducted by a Metrohm Autolab PGSTAT204 electrochemical station in a typical three-electrode mode, adopting a Pt electrode and a saturated Ag/AgCl electrode as the counter electrode and reference electrode, respectively. The electrolyte was 0.2 mol L^{-1} Na_2SO_4 aqueous solution with pH = 7.0. The Fluorine-doped Tin Oxide (FTO) glass coated with different photocatalysts was used as working electrode. 5.0 mg photocatalyst power samples were mixed with 280 μl ethanol and 20 μl Nafion under sonication for 30 min. The prepared mixture was dropped

onto conductive surface of FTO substrate (1.0 cm × 1.0 cm) and dried for 1 h. Electrochemical impedance spectroscopy (EIS) measurements were performed in the dark. The band positions of ZS-3 were measured by Mott-Schottky impedance-potential method with frequencies of 500, 1000 and 1500 Hz, respectively.

3. Results and discussion

3.1. Characterization

The rod-like ZIF-L obtained by reaction of $Zn(NO_3)_2$ and 2-MIM with the aid of PVP matched well with the ones reported in previous reference (Fu et al., 2018b), which was confirmed by both SEM image (Fig. S1a) and PXRD (Fig. S1b). Especially, the PXRD patterns reveal that all diffraction peaks of obtained ZIF-L fitted well to the simulated one (Chen et al., 2013; Fu et al., 2018b), indicating that rod-like ZIF-L with high purity is synthesized successfully.

The rod-like ZIF-L was sulfurized for a certain time to produce tube-like ZnS, which was defined as ZS-1, ZS-2, ZS-3 and ZS-6 for sulfurization 1 h, 2 h, 3 h, 6 h, respectively. As depicted in Fig. 1a, the PXRD patterns of ZS-1 and ZS-2 samples revealed that they are the matrix of incompletely sulfurized ZIF-L and ZnS, in which the characteristic peaks of both ZIF-L (11.1°, 17.2°, 18.2°, 28.0°, 29.2°) and ZnS (29.1°, 48.4°, 57.4°) were observed. The PXRD peaks at 29.1°, 48.4°, and 57.4° of ZS-3 and ZS-6 could be indexed to (111), (220) and (311) lattice planes of ZnS with cubic zinc blende structure (Lu et al., 2010), implying that the sulfurization of ZIF-L was complete and the expected ZnS with high purity was obtained. The component evolution of ZS-1, ZS-2, ZS-3 and ZS-6 was also investigated by FTIR (Fig. 1b). The spectrum of the ZIF-L demonstrated the absorption peaks at 418 cm^{-1}, 600-800 cm^{-1}, 900–1350 cm^{-1} and 1350-1500 cm^{-1} were assigned to Zn–N stretching, out-of-plane bending of the 2-MIM ring, in-plane bending of the 2-MIM ring and 2-MIM ring stretching, respectively (Fu et al., 2018b; Low et al., 2014b). It was observed that the characteristic peaks of ZIF-L were detected in the FTIR spectrum of ZS-1. All the characteristic peaks (especially the peak of Zn–N stretching bands at 418 cm^{-1}) of ZIF-L became weaker in ZS-2. The obvious single peak at 1654 cm^{-1} (C=O) for ZS-3 and ZS-6 was attributed to PVP (Sethia and Squillante, 2004; Wang et al., 2005) remained in the structure. This result corresponded well with the ZnS that reported in the previous reference (Lan et al., 2017).

The UV–vis DRS spectra (Fig. 1c) demonstrated that the pristine ZIF-L displayed selective light absorption in the region of 250 nm–300 nm, while the absorption edges of ZS-X were extended to 400 nm. The band gap (E_g) were estimated as 4.92 eV, 3.58 eV, 3.55 eV, 3.49 eV and 3.40 eV for the ZIF-L, ZS-1, ZS-2, ZS-3 and ZS-6, respectively, using $(Ah\nu)^2$ versus $h\nu$ (Qu et al., 2017) (A: the constant of absorbance, h: the Planck constant, ν: light frequency). The band gap of ZS-3 implied that ZnS derived from ZIF-L might be excited upon the irradiation of UV light (Zhang et al., 2007; Zhang and Martin, 2006).

From the SEM images as illustrated in Fig. 2a to Fig. 2d, it could be found that ZS-1, ZS-2 and ZS-3 exhibited rod-like shape with length of ca. 10 μm, while ZS-6 displayed as rod-like structure surrounded by ultra-fine particles. The tube-like structures of ZS-X were further observed via TEM (Fig. 2e and h). The hollow

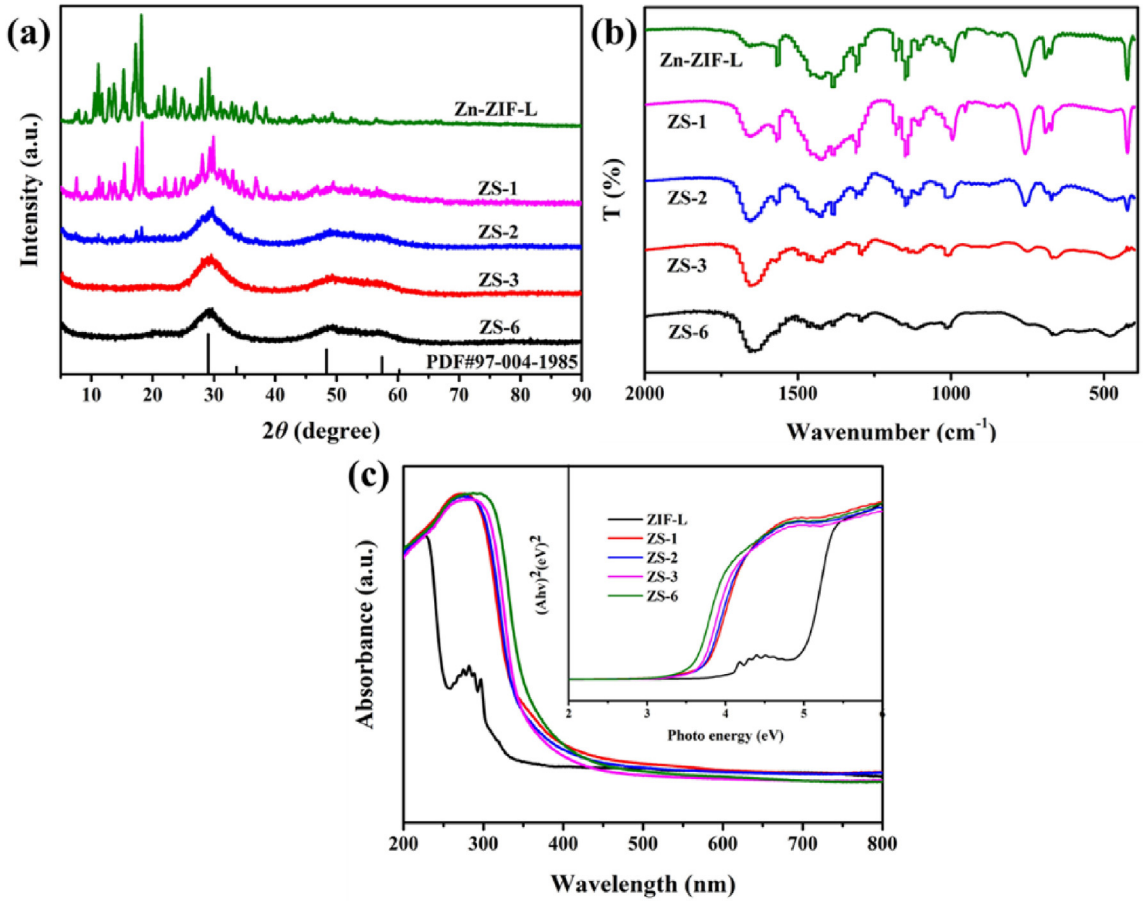

Fig. 1. (a) PXRD patterns, (b) FTIR spectra and (c) UV–vis DRS and E_g plot (inset) of ZIF-L and products of sulfurization.

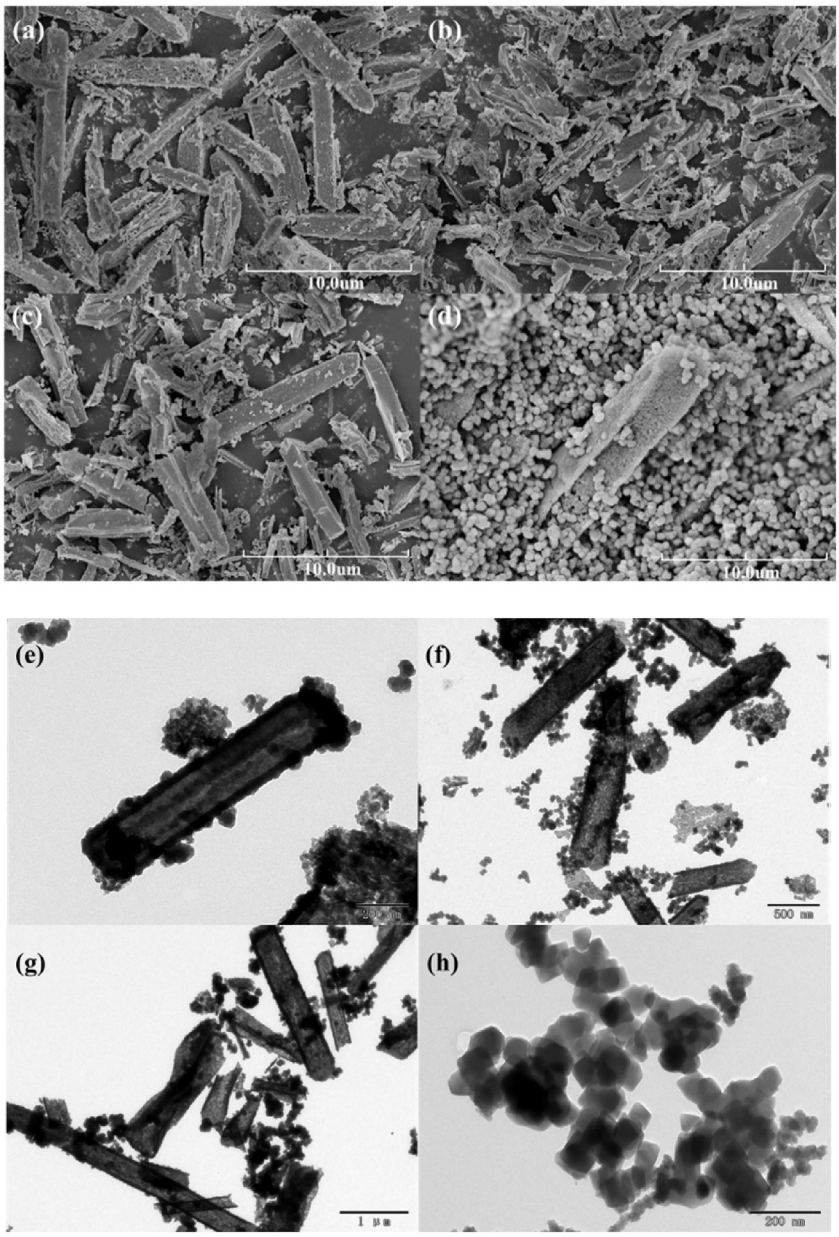

Fig. 2. SEM images of (a) ZS-1, (b) ZS-2, (c) ZS-3 and (d) ZS-6. TEM images of (e) ZS-1, (f) ZS-2, (g) ZS-3 and (h) ZS-6.

structures with thick wall and closed end were presented in ZS-1 and ZS-2. In ZS-3, the tube-like structure presented with open ends could be observed. However, as to ZS-6, it was found that the rod-like structure was surrounded by lots of fine particles, due to that the increase of sulfurization reaction time led to destroy and collapse of the hollow structure. The SEM-EDS (Fig. S2- Fig. S6) revealed the distribution of C, O, N, Zn, S elements, which further verified the formation process. The content of C, N and O (the characteristic element from ZIF-L) decreased and the ratio of Zn and S (the characteristic element from ZnS) elements were closer with the increase of sulfurization time. As depicted in Fig. S5 and Fig. S6, Zn and S elements were uniformly distributed throughout ZS-3 and ZS-6. The residual C and O in the structure are consistent with the FTIR results.

The isotropic and anisotropic chemical shift characterized by ^{13}C NMR can reflect the local environment of the nucleus in the sample. Solid-state NMR was introduced to detect the different properties of PVP, 2-MIM, ZIF-L, ZS-1, ZS-2, ZS-3, ZS-6 (Fig. 3). In the ^{13}C NMR spectra of PVP, the five-membered ring at around 10–50 ppm and the carbonyl peaks at around 175 ppm were observed, respectively, which corresponding with the reported literature (Ito et al., 2010). In the ^{13}C NMR spectra of 2-MIM, the peaks at around 144 ppm, 115 ppm and 14 ppm were attributed to the resonance signals of the N–C–N, N–C–C–N and $-CH_3$ (Morris et al., 2012; Niknam Shahrak et al., 2017). For ZIF-L, the resonances of N–C–N and N–C–C–N were weakened or shifted from 144 ppm to 150 ppm because the coordination of Zn–N bond; and the weak signal from carbonyl was also detected. The ^{13}C NMR spectra of ZS-1 and ZS-2 was similar to ZIF-L, but it can be noted that peaks originated from PVP at around 10–50 ppm were more obvious in ZS-2. The ^{13}C resonances representing PVP and 2-MIM at 10–50 ppm, 115 ppm, 175 ppm were observed in ZS-3 and in ZS-6 NMR spectra, indicating that there was small quantity of PVP and residual 2-MIM in the structure. It was reported that there are some free 2-MIMs located between the

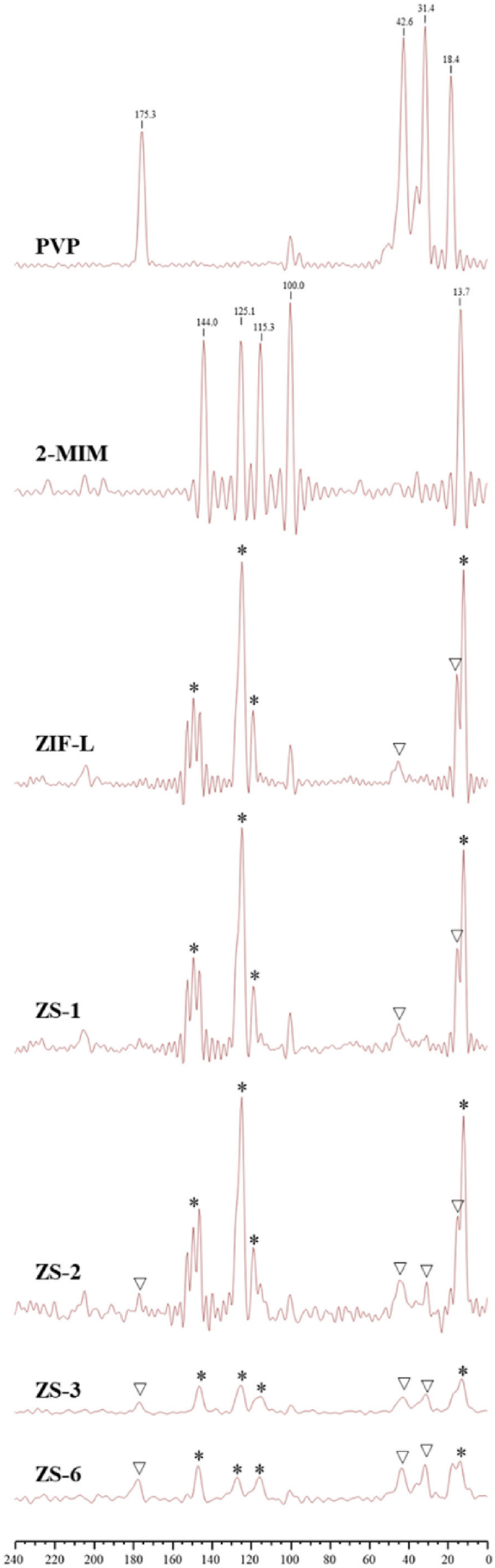

Fig. 3. The ^{13}C NMR spectra of PVP, 2-MIM, ZIF-L, ZS-1, ZS-2, ZS-3 and ZS-6. *Stars* (*) indicate resonance peaks originated from 2-MIM, *triangles* (▽) indicate resonance peaks originated from PVP.

adjacent ZIF-L layers to stabilize the structure via hydrogen bonding interactions (Low et al., 2014a). With the extension of sulfurization duration, the contents of 2-MIM coordinated to Zn^{2+} decreased gradually. When the sulfurization was complete (like ZS-3 and ZS-6), all 2-MIMs coordinated to Zn^{2+} were replaced by S element. The existence of minor free 2-MIM and PVP could be detected by ^{13}C NMR spectra with ultrahigh precision, which however couldn't be observed by FTIR and EDS.

The formation mechanism of porous tube-like ZnS was proposed as the illustration in Scheme S2. The S^{2-} ions formed from the hydrolysis of TAA under 30 °C (pH = 8.07) react competitively with Zn^{2+} of Zn—N in the ZIF-L's surface to form ZnS (Jiang et al., 2012), as listed in Equation (3) (Kaewanan et al., 2017; Su et al., 2001). In detail, S^{2-} firstly reacted with Zn^{2+} released from the outer surface of ZIF-L, and the thin ZnS wall was generated with the aid of the adhesive action of PVP. Then, the 2-MIM inside ZIF-L was gradually replaced by S^{2-}, and the internal Zn^{2+} diffused to the outside to form ZnS with a porous tube-like structure (Fu et al., 2018a; Jiang et al., 2012; Yu et al., 2009).

$$CH_3CSNH_2 + OH^- + Zn^{2+} \rightarrow CH_3COONH_4 + ZnS \quad (3)$$

3.2. Photocatalytic activity

The photocatalytic Cr(VI) reduction and X—3B degradation performances of the prepared ZS-X samples were carried out under UV light irradiation (Fig. 4a and b). Under the dark condition, the Cr(VI) and X—3B adsorption efficiencies over ZS-3 were 24.19% and 8.1% within 100 min, respectively, indicating that the adsorption-desorption equilibrium was achieved in 60 min. After achieving the adsorption-desorption equilibrium toward X—3B, ZS-3 exhibited the highest efficiency (94.6% at 20 min, 97.7% within 40 min), followed by ZS-6 (91.1% at 20 min, 96.3% within 40 min), ZS-2 (89.3% at 20 min, 97.2% within 40 min), ZS-1 (73.7% at 20 min, 92.1% within 40 min) and ZIF-L (26.9% at 20 min, 42.1% within 40 min), as illustrated in Fig. 4a. As to the photocatalytic Cr(VI) reduction (Fig. 4b), the highest reduction efficiency was accomplished by ZS-6 (100% within 20 min), followed by ZS-3 (97.5% at 20 min), ZS-2 (90.2% at 20 min), ZS-1 (53.3% with 40 min) and ZIF-L (11.3% within 40 min). It was obvious that the ZnS-X photocatalysts displayed higher photocatalytic activities towards Cr(VI) reduction and X—3B degradation than those of either ZIF-L or ZIF-L/ZnS mixture. As well, the pseudo-first order model ($\ln(C/C_0) = kt$) was used to study the kinetic curves for photocatalytic activities, in which k is the apparent rate constant (min^{-1}) (Liu et al., 2018; Wang et al., 2018). The k values were presented in Fig. 4c and d and , in which the X—3B degradation rates exhibited a volcano-shaped curve (ZS-3 at the peak), while the Cr(VI) reduction rates followed the order of ZS-6 > ZS-3 > ZS-2 > ZS-1 > ZIF-L.

It was demonstrated that BET specific surface areas of ZS-1, ZS-2 and ZS-3 increased from 40.93 to 81.27 $m^2 g^{-1}$ along with the increasing pore volume (Fig. S8 and Table S1), which were larger than those of ZnS prepared via other methods (Table S2). The further thermal treatment toward the sample like ZS-6 resulted into slight decrease of surface area and pore volume, due to the destroy and collapse of the hollow structure (Table S1). It was concluded that the larger specific surface area and pore volume of the ZS-3 achieved it exposing more active sites (Zheng et al., 2010),

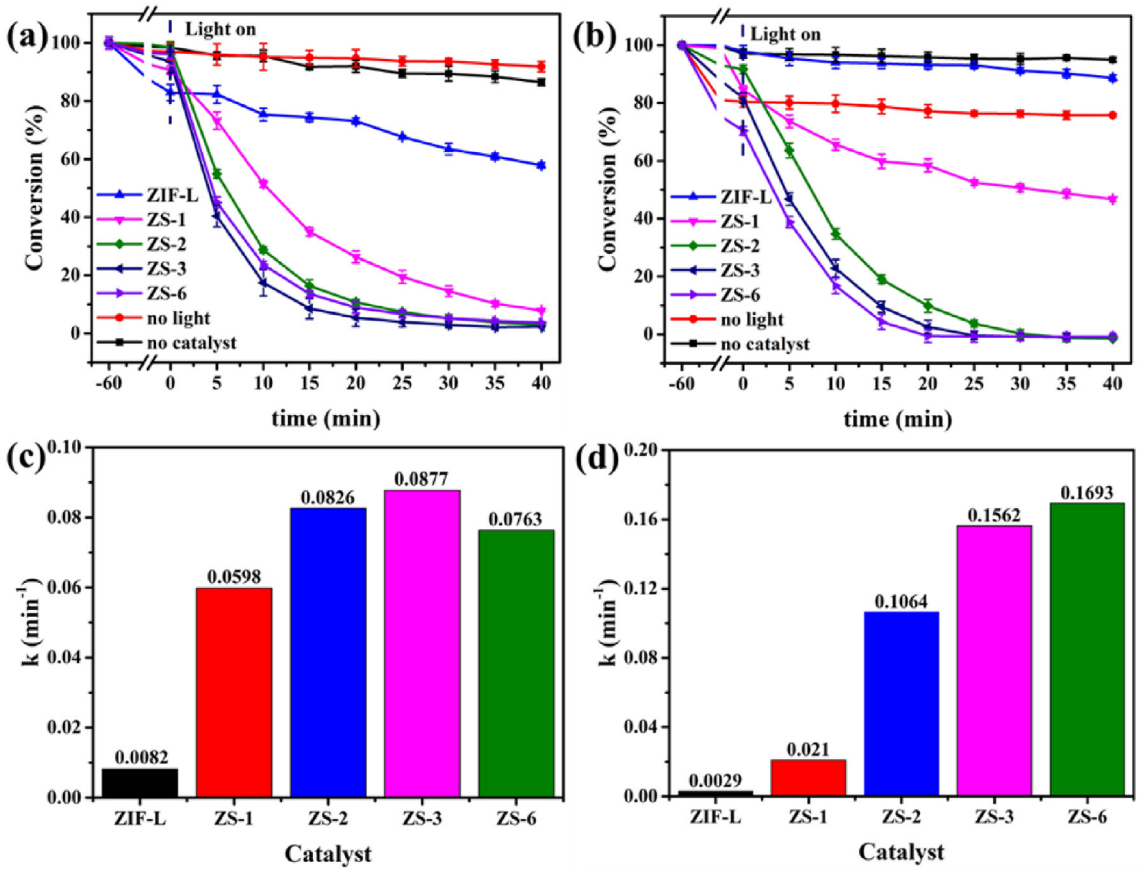

Fig. 4. Photocatalytic (a) X−3B degradation and (b) Cr(VI) reduction performances of ZIF-L and products of sulfurization (ZS-1, ZS-2, ZS-3, ZS-6) under UV light. Rate constant *k* of (c) X−3B degradation and (d) Cr(VI) reduction.

which is beneficial for photocatalytic Cr(VI) reduction and X−3B degradation. Considering that ZS-3 possessed good morphology and photocatalytic performances, it was selected to conduct subsequent experiments to investigate the influences of pH and co-existing ions toward its photocatalytic performances.

3.2.1. Photocatalytic Cr(VI) reduction

Previous researches have displayed that pH value of solution can influence the Cr(VI) reduction rate (Padhi and Parida, 2014). Generally, the lower pH is favorable for Cr(VI) reduction (Shi et al., 2011). However, considering that most wastewater was neutral and weakly acidic and ZnS might be unstable at strongly acidic conditions (pH = 2.0 or 3.0), in this study, the pH was adjusted respectively to 4.0, 6.0, 8.0 and 10.0 with the aid of H_2SO_4 or NaOH solutions with suitable concentration (Zhou and Guzman, 2016). The effects of initial pH values on Cr(VI) reduction activities are depicted in Fig. 5a, in which it was found that lower pH (4.0) favored the Cr(VI) transformation into Cr(III).

The zeta potential of ZS-3 decreased with the increase of pH (Fig. 5b), which leads to declined Cr(VI) adsorption due to stronger charge repulsion (Zhou and Guzman, 2014). Meanwhile, the photocatalytic Cr(VI) reduction efficiencies increased with the decrease of pH values. Under acidic conditions, the primary Cr(VI) species in aqueous solution are $HCrO_4^-$ and $Cr_2O_7^{2-}$ (Guo et al., 2019; Ku and Jung, 2001). Equations (4) and (5) represent the photocatalytic Cr(VI) reduction under acid conditions (Wang et al., 2016a), in which the abundant H^+ could further contribute to the reduction from Cr(VI) to Cr(III). In alkaline medium, the predominant Cr(VI) species are CrO_4^{2-} (Lee et al., 2018; Zhao et al., 1998), and the reaction process follows Equations (5) and (6) (Wang et al., 2016a; Wang et al., 2019). However, the difference was not obvious for the Cr(VI) reduction under the condition of pH being 4.0, 6.0, and 8.0. In contrast, the efficiency decreased from 100.0% at pH being 4.0−81.6% at pH being 10.0, which could be ascribed to the possible mask of the active sites of ZS-3 by the formed $Cr(OH)_3$ precipitates (Wang et al., 2015). The results indicated that ZS-3 exhibited good photocatalytic performance toward Cr(VI) reduction under weakly acidic and neutral conditions.

$$14H^+ + Cr_2O_7^{2-} + 6e^- \rightarrow 2Cr^{3+} + 7H_2O \quad (4)$$

$$2H_2O + 2h^+ \rightarrow H_2O_2 + 2H^+ \quad (5)$$

$$CrO_4^{2-} + 4H_2O + 3e^- \rightarrow Cr\left(OH\right)_3\left(s\right) + 5OH^- \quad (6)$$

The Cr(VI) reduction efficiencies of ZS-3, P_{25} (commercial TiO_2) and commercial ZnS are investigated, indicating that P_{25} and commercial ZnS achieved only 10.6% and 10.0% Cr(VI) reduction under UV light irradiation, respectively (Fig. 5c). In contrast, 100% Cr(VI) reduction was accomplished within 30 min using ZS-3 as photocatalyst. It was worthy to noting that the Cr(VI) reduction efficiency was negligible under UV light illumination without any photocatalyst, implying that Cr(VI) reduction with the presence of both UV light and ZS-3 was a photocatalytic process (Wang et al., 2017). The apparent quantum efficiency (AQE) of Cr(VI) reduction at different wavelengths, a key index of evaluating photocatalytic activities (Murphy and Buriak, 2015), was demonstrated in Fig. 5

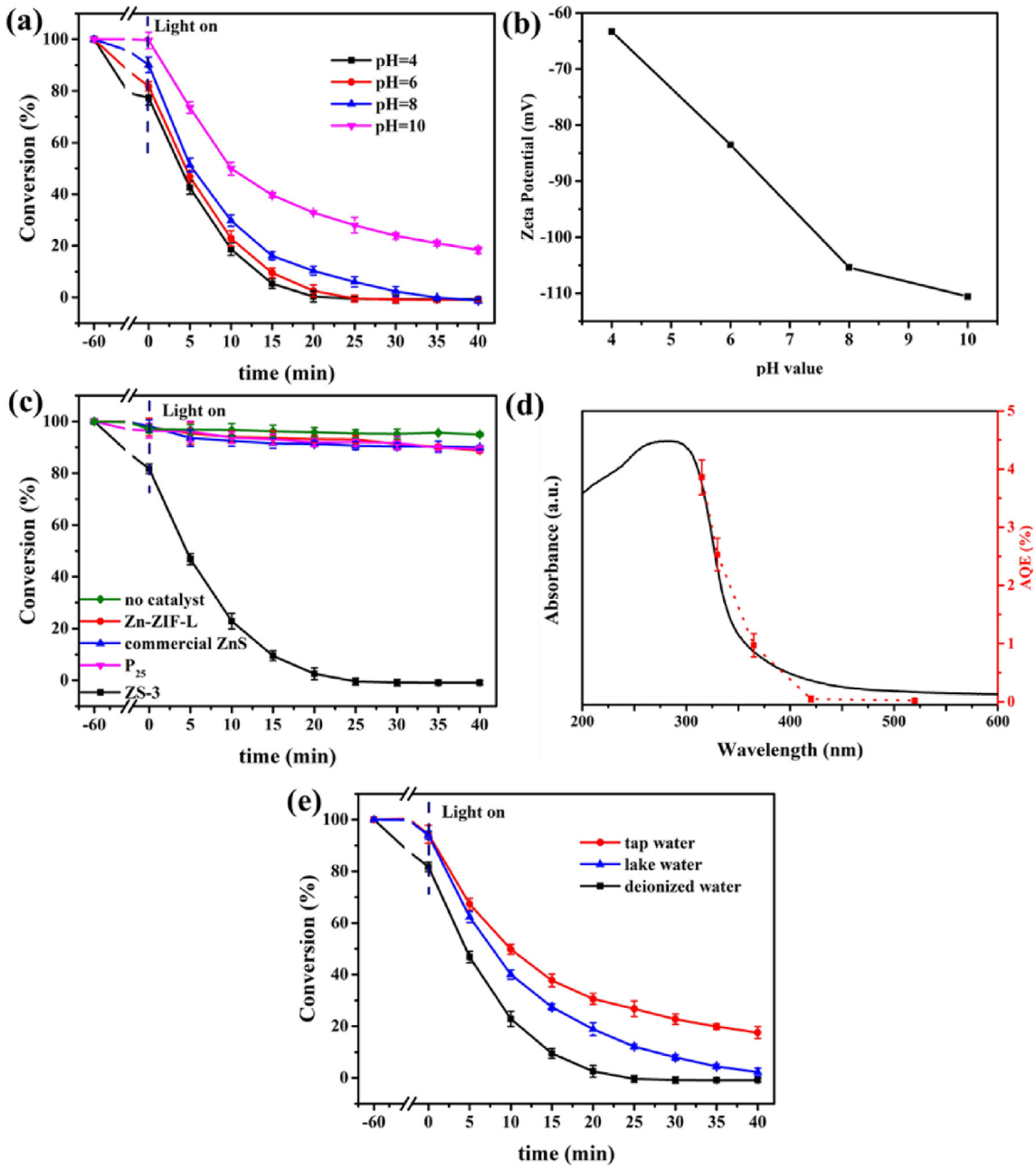

Fig. 5. (a) Effect of different pH values on reduction of Cr(VI) (b) The zeta potential of ZS-3 at different pH values. (c) Photocatalytic Cr(VI) removal performance over commercial ZnS, P_{25} and ZS-3. (d) Apparent quantum efficiency (AQE) of Cr(VI) reduction over ZS-3 at various monochromatic light corresponding to the absorption spectrum. (e) Effects of foreign ions (initial pH = 7.3 and 7.4 in tap water and lake water, respectively) on Cr(VI) reduction. Experimental conditions: 40.0 mg photocatalyst, 200 mL Cr(VI) (20 mg L^{-1}).

(d). The AQEs of ZS-3 were 3.86%, 2.53%, 0.97%, 0.05% and 0.02% at 315 nm, 330 nm, 365 nm, 420 nm and 520 nm, which matched well with the curve trend of UV–vis DRS spectra. This further indicated that Cr(VI) reduction was a photo-induced action (Hoque and Guzman, 2018; Li et al., 2019; Ouyang and Ye, 2011).

According to reported studies (Abdullah et al., 1990; Sun et al., 2005; Wang et al., 2000), the photocatalytic efficiencies will be influenced by foreign ions including inorganic salts and organic matters. For practical purpose, the ZS-3 photocatalyst was used to treat the simulated wastewater containing Cr(VI) prepared with real lake water (Table S3) and tap water (Table S3) instead of ultrahigh water. The results revealed that 82.5% and 97.8% Cr(VI) reductions were achieved in real tap water solution (pH = 7.4) and lake water solution (pH = 7.3) within 40 min after UV light irradiation (Fig. 5e). The obvious declining Cr(VI) reduction in tap water solution was contributed to the negative impact of co-existing inorganic ions like K^+, Na^+, Ca^{2+}, Mg^{2+}, SO_4^{2-}, Cl^-, NO_3^-, PO_4^{3-}, which was similar to the previous reports (Yi et al., 2019). While, the slight decrease of Cr(VI) reduction efficiency in real lake water could be assigned to the balance of negative impact of inorganic ions and positive effect of organic matters (consuming the photo-induced holes) (Djellabi and Ghorab, 2015; Yi et al., 2019; Yin et al., 2018). Based on the above-stated experiment results, it was concluded that ZS-3 can be potentially used as photocatalyst to treat real wastewater containing Cr(VI) pollutant.

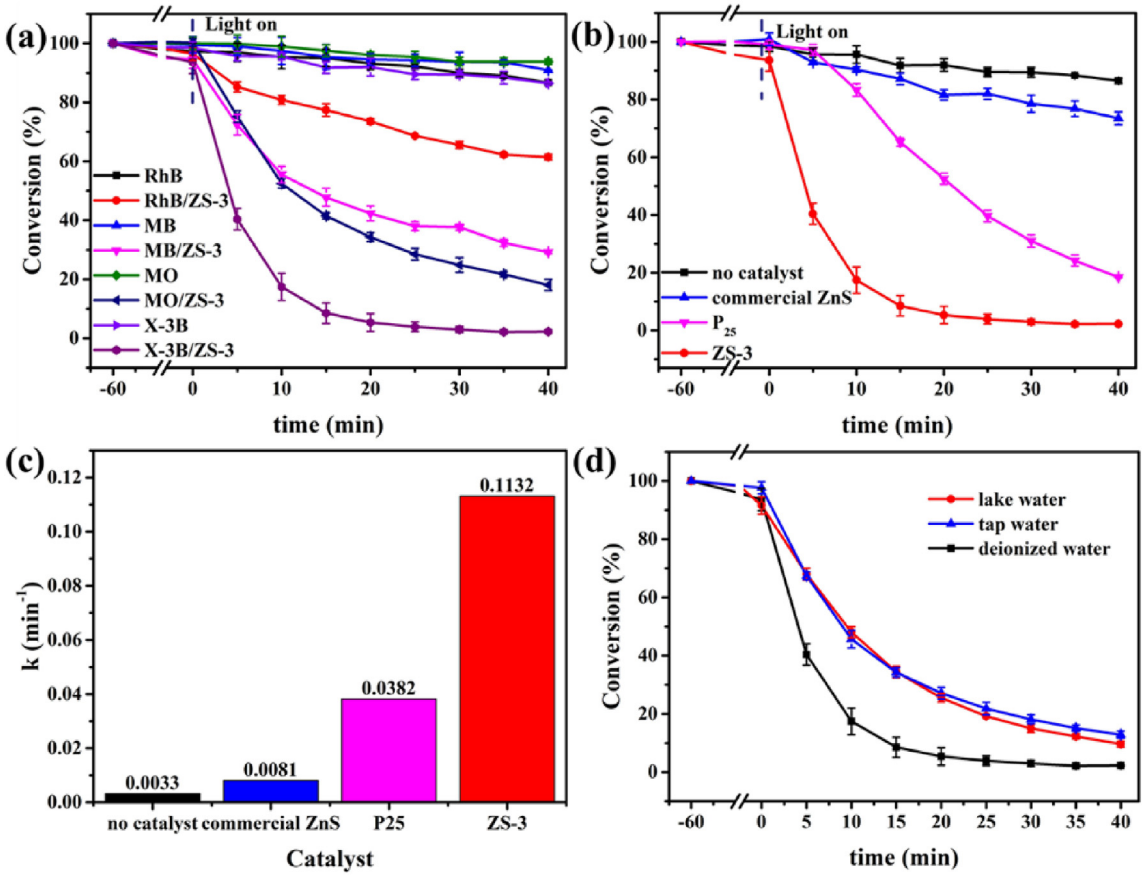

Fig. 6. (a) Photocatalytic degradation of RhB (10 mg L^{-1}), MB (10 mg L^{-1}), MO (10 mg L^{-1}) and X−3B (50 mg L^{-1}) solutions over ZS-3. Initial pH: RhB 4.9, MB 5.4, MO 5.7, X−3B 4.6. Reaction conditions: 40 mg photocatalyst, 200 mL RhB, MB, MO, and X−3B. (b) Photocatalytic X−3B degradation over different photocatalysts under UV light. (c) Rate constant *k* of X−3B degradation over different photocatalysts (d) Effects of foreign ions on X−3B degradation. Experimental conditions: 40 mg photocatalyst, 200 mL X−3B aqueous solution.

3.2.2. Photocatalytic organic pollutants degradation

To further investigate the photocatalytic oxidation capacity of ZS-3, some organic dyes like RhB, MB, MO and X−3B were considered as organic pollutant models to conduct photocatalytic experiments (Fig. 6a). In the presence of ZS-3, photocatalytic decomposition efficiencies toward RhB (10 mg L^{-1}, pH = 4.9), MB (10 mg L^{-1}, pH = 5.4), MO (10 mg L^{-1}, pH = 5.7) and X−3B (10 mg L^{-1}, pH = 4.6) were 38.6%, 70.8%, 81.9%, 97.7% after 40 min's UV irradiation. For comparison, only ca. 16.9% RhB, 10.5% MB, 10.4% MO and 16.9% X−3B were degraded under UV light in the absence of photocatalyst within 40 min. The apparent quantum efficiencies (AQE) of X−3B degradation at 315 nm and 330 nm wavelength within 15 min, 30 min as well as 45 min was listed in Table S4. It was demonstrated that AQEs decreased with increasing time at single wavelength, and AQE value at 315 nm was higher than that at 330 nm with the same time.

As demonstrated in Fig. 6b, in the absence of photocatalysts, X−3B was degraded by 13.5% under UV irradiation after 40 min. With commercial ZnS and P_{25} as photocatalysts, the photocatalytic efficiencies were 26.5% and 81.5% up to 40 min, respectively. In comparison, ZS-3 achieved 97.7% degradation efficiency with reaction rate of 0.1132 min^{-1} (Fig. 6c) within 40 min under the same conditions, which was quicker than that of P_{25} ($k = 0.0382$ min^{-1}). The EIS measurements were carried out to further verify the degradation efficiency differences between ZS-3, P_{25} as well as commercial ZnS (Fig. S9). Generally, the smaller arc radius in Nyquist plot represents the lower charge transfer resistance (R_{ct}) values (Cao et al., 2017; Lan et al., 2017; Qiu et al., 2018). Compared with P_{25} and commercial ZnS, the arc radius of ZS-3 is smaller, which demonstrated the more effective separation of the photogenerated charge carriers and enhanced photocatalytic performances.

The X−3B aqueous solution prepared with lake water and tap water instead of deionized water was adopted to clarify the influence of foreign ions on organic pollutant degradation, which revealed that the degradation efficiencies of X−3B in lake water and tap water are 90.3% and 87.1%, respectively (Fig. 6d). It could be concluded that the foreign ions also have no significant influence on the X−3B degradation. For comparison, the photocatalytic Cr(VI) reduction or X−3B degradation activities of ZS-3 and different ZnS photocatalysts in previously reported literatures are listed in Table S5. The results confirmed that ZS-3 possessed superiorly photocatalytic performances toward both Cr(VI) reduction and X−3B degradation.

Considering the possible coexistence of Cr(VI) and organic pollutants in real industrial wastewater, the simultaneously photocatalytic treatments toward Cr(VI) reduction and organic pollutant degradation over ZS-3 were performed in a Cr(VI)/X−3B matrix (initial pH = 6.0). As shown in Fig. 7a, photocatalytic efficiencies of Cr(VI) reduction and organic pollutant degradation were 100.0% and 97.7% in the mono-component system. In the matrix system, the Cr(VI) reduction rate declined from 0.1563 min^{-1} to 0.0902 min^{-1} (Fig. S10), despite that the efficiency of Cr(VI) removal was still 100% within 40 min. While photocatalytic X−3B degradation

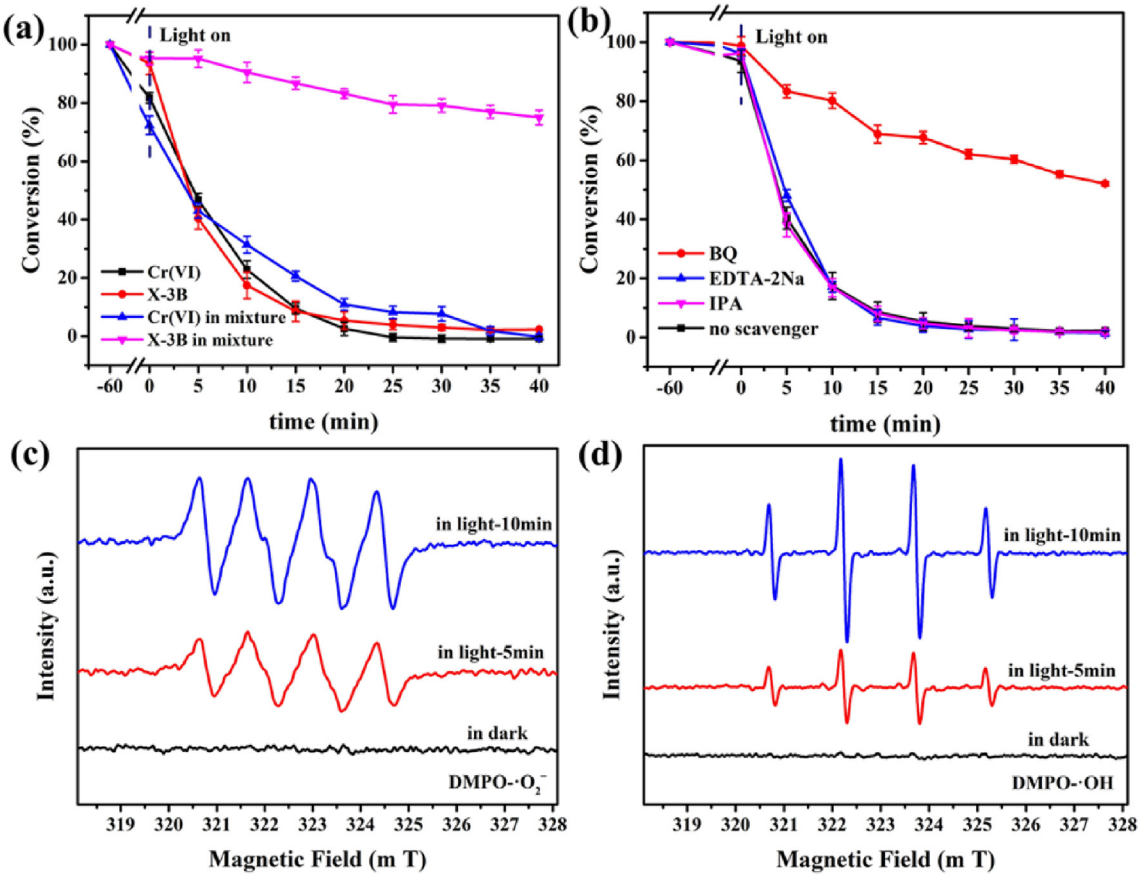

Fig. 7. (a) Photocatalytic Cr(VI) reduction and degradation of X−3B in mono-system and mixed system. Conditions: 40 mg photocatalyst, 200 mL of Cr(VI) (20 mg L^{-1}) and X−3B (50 mg L^{-1}), pH = 6.0. (b) Effects on X−3B degradation with different hole scavengers. The ESR spectra of active species trapped by DMPO in aqueous dispersion for $\cdot O_2^-$ (c) and ·OH (d) over ZS-3.

efficiency decreased from 97.7% to 25.0%. It was implied that Cr(VI) reduction and X−3B degradation might be competitive in the matrix.

3.2.3. Photocatalytic mechanism

In order to explore the photocatalytic mechanism, a series of active species capture agents including benzoquinone (BQ) (Ju et al., 2017), isopropyl alcohol (IPA) (Yi et al., 2019) and EDTA-2Na (Yi et al., 2019) with concentrations of 0.2 mmol L^{-1} were selected to capture $\cdot O_2^-$, ·OH and h^+, respectively. As illustrated in Fig. 7b, when BQ was added into the photocatalytic system, the X−3B photocatalytic degradation rate decreased to 57.7%. However, the addition of IPA and EDTA-2Na exerted no noticeable inhabitation to the X−3B degradation. The active species capture results implied that $\cdot O_2^-$ rather than ·OH and h^+ was the primary active specie to decompose X−3B. The Cr(VI) reduction is generally considered to be a process of electron transfer (Liu et al., 2012). According to previous reports, $\cdot O_2^-$ generated by reaction between photo-induced electrons on CBs and dissolved oxygen can also participate in the process of Cr(VI) to Cr(III) transformation (Tartour and Zitvogel, 2013; Wang et al., 2016; Zhang et al., 2018). Under the N_2 atmosphere (Fig. S15), the photocatalytic efficiency toward Cr(VI) declined from 100.0% under air atmosphere to 81.2% within 25 min, which was similar to the previous reports (Yi et al., 2019). In the Cr(VI) and X−3B matrix, the X−3B degradation efficiency decreased from 97.7% in single X−3B solution to 25.0%, and the Cr(VI) reduction efficiency rate decreased from 0.1563 min^{-1} in the individual Cr(VI) solution to 0.0902 min^{-1} with nearly 100% reduction efficiencies within 40 min. If the reaction time was prolonged, X−3B was further degraded when Cr(VI) was completely reduced (Fig. S16), indicating that $\cdot O_2^-$ preferred to accomplish Cr(VI) reduction instead of X−3B (Gadhi et al., 2016) in the matrix system. The above experiments proved that $\cdot O_2^-$ does participate in the Cr(VI) reduction. However, it can be seen from the N_2 experiment that Cr(VI) can still be reduced without dissolved oxygen, indicating that the removal of Cr(VI) was attributed to both $\cdot O_2^-$ and photo-induced electrons on CB (Hu et al., 2014).

The ESR measurement was carried out to determine the formation of active species over ZS-3 in the process of photocatalytic experiments. According to Fig. 7c and d, both signals of DMPO-$\cdot O_2^-$ and DMPO-·OH were observed under UV irradiation for 5 min and 10 min, while no obvious signals were detected in dark, demonstrating that $\cdot O_2^-$ and ·OH were produced during the photocatalytic process. However, in the active species capture experiment for photocatalytic X−3B degradation, the addition of IPA as ·OH scavenger exerted minor effect on the degradation efficiency, indicating that the formed ·OH didn't participate in the degradation of X−3B.

Photocatalytic mechanism over ZS-3 was also investigated by electrochemical tests. As demonstrated in Fig. 8a, slope of C^2 value versus potential in Mott−Schottky measurements was positive, confirming that ZS-3 was the n-type semiconductor (Spagnol et al., 2009). The conduction band (CB) of ZS-3 determined by Mott-Schottky tests was ca. −1.21 eV *versus* the Ag/AgCl electrode at pH = 7.0. The valence band (VB) potential value of ZS-3 was calculated as 2.48 eV *vs*. NHE ($E_{CB} = E_{VB} - E_g$) (Zou et al., 2016) based on the band gap of 3.49 eV.

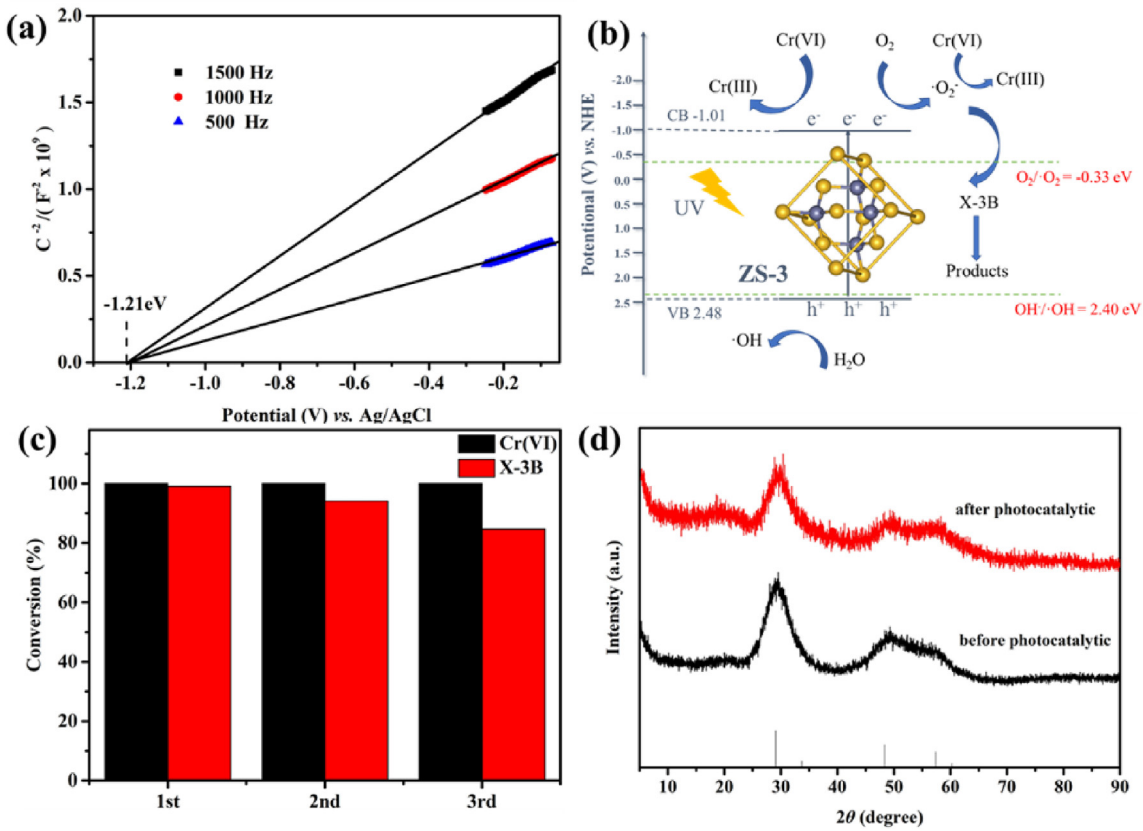

Fig. 8. (a) Mott-Schottky curves of ZS-3 at different frequencies. (b) A proposed reaction mechanism toward photocatalytic Cr(VI) reduction and X−3B degradation of ZS-3. (c) The cyclic performance of Cr(VI) reduction and X−3B degradation over ZS-3. (d) PXRD patterns of ZS-3 before and after three cycles for photocatalytic performance.

As the redox potential value of CB (−1.01eV *vs*. NHE) is higher than that of $O_2/\cdot O_2^-$ (−0.33 eV *vs*. NHE), it is reasonable that abundant $\cdot O_2^-$ radicals were produced (Dong and Zhang, 2013). Otherwise, ·OH produced by hole oxidation in the valence band (VB) might enhance the separation of electrons and holes, but played little role in transformation from Cr(III) to Cr(VI). On the basis of this fact, it is proposed that e^- and $\cdot O_2^-$ could simultaneously reduce Cr(VI), and $\cdot O_2^-$ can also oxidize X−3B in single system (Fig. 8b). However, in the matrix system, $\cdot O_2^-$ radicals were more inclined to participate in the Cr(VI) reduction than X−3B degradation, which led to significant inhabitation toward X−3B and minor restriction toward Cr(VI).

3.2.4. Reusability and stability of ZS-3

In order to evaluate the practical application, the reusability and stability over ZS-3 were investigated. The repeated usage cycles experiments were conducted under the identical conditions. As depicted in Fig. 8c, the Cr(VI) reduction efficiency was maintained as 100.0% and the X−3B degradation efficiency decreased from 100.0% to 84.7% after three cycles, illustrating that ZS-3 could be reusable. Furthermore, the PXRD pattern of ZS-3 after photocatalytic reaction matched perfectly with the original sample and the simulated one (Fig. 8d), and it can be seen from SEM and TEM that the morphology of ZS-3 experienced no noticeable changes (Fig. S11), which indicated that ZS-3 is stable in the process of photocatalytic activities.

4. Conclusions

The porous tube-like ZnS (especially ZS-3) was facilely prepared from the rod-like ZIF-L as precursor, which exhibited better photocatalytic Cr(VI) reduction and dye degradation performances under UV light than both P_{25} and ZnS synthesized by other methods. The AQE results demonstrated high photocatalytic efficiencies of ZS-3. The influence factors like pH and foreign matters in tap water and lake water on the photocatalytic performances were explored. The positions of CB and VB were determined by Mott-Schottky curve along with the ESR determination, which confirmed the proposed photocatalysis mechanism. The cycling experiments demonstrated that ZS-3 has the characteristics of reusability and stability. ZnS might react with many other metals to form precipitates with lower K_{sp}, which would influence its speciation, mobility and bioavailability in real environment. Fortunately, ZnS is non-toxic and harmless as a photocatalyst, exerting no impact and threat to the environment. This work also demonstrated that some sulfide photocatalysts with particular morphology and enhanced photocatalytic performances could be fabricated from the tunable metal-organic frameworks.

Declaration of competing interest

On behalf of all authors, I declare that we do not have any commercial or associative interest that represents a conflict of interest in connection with the work entitled “Porous tube-like ZnS derived from rod-like ZIF-L for photocatalytic Cr(VI) reduction and organic pollutants degradation”.

Acknowledgements

This work was supported by National Natural Science

Foundation of China (51878023, 51578034), Great Wall Scholars Training Program Project of Beijing Municipality Universities (CIT&TCD20180323), Project of Construction of Innovation Teams and Teacher Career Development for Universities and Colleges Under Beijing Municipality (IDHT20170508), Beijing Talent Project (2018A35).

Appendix A. Supplementary data

Supplementary data to this article can be found online at https://doi.org/10.1016/j.envpol.2019.113417.

References

Abdullah, M., Low, G.K.C., Matthews, R.W., 1990. Effects of common inorganic anions on rates of photocatalytic oxidation of organic carbon over illuminated titanium dioxide. J. Phys. Chem. 94, 6820–6825.
Adeyemo, A.A., Adeoye, I.O., Bello, O.S., 2012. Metal organic frameworks as adsorbents for dye adsorption: overview, prospects and future challenges. Toxicol. Environ. Chem. Rev. 94, 1846–1863.
Ao, Y., Xu, J., Fu, D., Shen, X., Yuan, C., 2008. Low temperature preparation of anatase TiO_2-activated carbon composite film. Appl. Surf. Sci. 254, 4001–4006.
Babel, S., Kurniawan, T.A., 2004. Cr(VI) removal from synthetic wastewater using coconut shell charcoal and commercial activated carbon modified with oxidizing agents and/or chitosan. Chemosphere 54, 951–967.
Cao, Y., Xia, Y., Cheng, J., Zheng, H., Chen, Y., 2017. A novel visible-light-driven In-based MOF/graphene oxide composite photocatalyst with enhanced photocatalytic activity toward the degradation of amoxicillin. Appl. Catal. B Environ. 200, 673–680.
Chao, W., Ao, Y., Wang, P., Zhang, S., Jin, Q., Hou, J., 2010. A simple method for large-scale preparation of ZnS nanoribbon film and its photocatalytic activity for dye degradation. Appl. Surf. Sci. 256, 4125–4128.
Chen, R., Yao, J., Gu, Q., Smeets, S., Baerlocher, C., Gu, H., Zhu, D., Morris, W., Yaghi, O.M., Wang, H., 2013. A two-dimensional zeolitic imidazolate framework with a cushion shaped cavity for CO_2 adsorption. ChemComm 49, 9500–9502.
Costa, M., 1997. Toxicity and carcinogenicity of Cr(VI) in animal models and humans [Review]. Crit. Rev. Toxicol. 27, 431–442.
Demirbas, E., Kobya, M., Senturk, E., Ozkan, T., 2004. Adsorption kinetics for the removal of chromium (VI) from aqueous solutions on the activated carbons prepared from agricultural wastes. Water S.A. 30, 533–539.
Devulapalli, A.R., Choi, J., Lee, S., Ma, R., Kim, T., 2015. Self-assembled macro porous ZnS-graphene aerogels for photocatalytic degradation of contaminants in water. RSC Adv. 5, 18342–18351.
Djellabi, R., Ghorab, M.F., 2015. Photoreduction of toxic chromium using TiO_2-immobilized under natural sunlight: effects of some hole scavengers and process parameters. Desalination and Water Treatment 55, 1900–1907.
Dong, G., Zhang, L., 2013. Synthesis and enhanced Cr(VI) photoreduction property of formate anion containing graphitic carbon nitride. J. Phys. Chem. C 117, 4062–4068.
Drobek, M., Kim, J.-H., Bechelany, M., Vallicari, C., Julbe, A., Kim, S.S., 2016. MOF-based membrane encapsulated ZnO nanowires for enhanced gas sensor selectivity. ACS Appl. Mater. Interfaces 8, 8323–8328.
Du, X.D., Wang, C.C., Liu, J.G., Zhao, X.D., Zhong, J., Li, Y.X., Li, J., Wang, P., 2017. Extensive and selective adsorption of ZIF-67 towards organic dyes: performance and mechanism. J. Colloid Interface Sci. 506, 437–441.
Eggins, B.R., Robertson, P.K.J., Murphy, E.P., Woods, E., Irvine, J.T.S., 1998. Factors affecting the photoelectrochemical fixation of carbon dioxide with semiconductor colloids. J. Photochem. Photobiol. A Chem. 118, 31–40.
Eggins, B.R., Robertson, P.K.J., Stewart, J.H., Woods, E., 1993. Photoreduction of carbon dioxide on zinc sulfide to give four-carbon and two-carbon acids. J. Chem. Soc., Chem. Commun. 349–350.
Fang, X., Zhai, T., Gautam, U.K., Li, L., Wu, L., Bando, Y., Golberg, D., 2011. ZnS nanostructures: from synthesis to applications. Prog. Mater. Sci. 56, 175–287.
Fu, H., Wang, X., Wang, P., Wang, Z., Ren, H., Wang, C.-C., 2018a. Enhanced acetone sensing performance of Au nanoparticle modified porous tube-like ZnO derived from rod-like ZIF-L. Dalton Trans. 47, 9014–9020.
Fu, H., Wang, Z., Xun, W., Peng, W., Wang, C.C., 2018b. Formation mechanism of rod-like ZIF-L and fast phase transformation from ZIF-L to ZIF-8 with morphology changes controlled by polyvinylpyrrolidone and ethanol. CrystEngComm 20, 1473–1477.
Gadhi, T.A., Hernández-Gordillo, A., Bizarro, M., Jagdale, P., Tagliaferro, A., Rodil, S.E., 2016. Efficient α/β-Bi_2O_3 composite for the sequential photodegradation of two-dyes mixture. Ceram. Int. 42, 13065–13073.
Galán, B., Castañeda, D., Ortiz, I., 2005. Removal and recovery of Cr(VI) from polluted ground waters: a comparative study of ion-exchange technologies. Water Res. 39, 4317–4324.
Gheju, M., Balcu, I., 2011. Removal of chromium from Cr(VI) polluted wastewaters by reduction with scrap iron and subsequent precipitation of resulted cations. J. Hazard Mater. 196, 131–138.
Gu, H., Rapole, S.B., Huang, Y., Cao, D., Luo, Z., Wei, S., Guo, Z., 2013. Synergistic interactions between multi-walled carbon nanotubes and toxic hexavalent chromium. J. Mater. Chem. 1, 2011–2021.
Guo, J., Li, J.-J., Wang, C.-C., 2019. Adsorptive removal of Cr(VI) from simulated wastewater in MOF BUC-17 ultrafine powder. J. Environ. Chem. Eng. 7, 102909.
Guzman, M.I., Martin, S.T., 2008. Oxaloacetate-to-malate conversion by mineral photoelectrochemistry: implications for the viability of the reductive tricarboxylic acid cycle in prebiotic chemistry. Int. J. Astrobiol. 7, 271–278.
Guzman, M.I., Martin, S.T., 2009. Prebiotic metabolism: production by mineral photoelectrochemistry of α-ketocarboxylic acids in the reductive tricarboxylic acid cycle. Astrobiology 9, 833–842.
Guzman, M.I., Martin, S.T., 2010. Photo-production of lactate from glyoxylate: how minerals can facilitate energy storage in a prebiotic world. Chem. Commun. 46, 2265–2267.
Hörner, G., Johne, P., Künneth, R., Twardzik, G., Roth, H., Clark, T., Kisch, H., 2015. Semiconductor type A photocatalysis: role of substrate adsorption and the nature of photoreactive surface sites in zinc sulfide catalyzed C–C coupling reactions. Chem. Eur J. 5, 208–217.
Hao, Z., Song, X., Min, Z., Xing, M., Zhao, S., Su, S., Yang, W., Song, S., Zhang, H., 2013. One-dimensional channel-structured Eu-MOF for sensing small organic molecules and Cu^{2+} ion. J. Mater. Chem. 1, 11043–11050.
Henglein, A., Gutiérrez, M., Fischer, C.H., 1984. Photochemistry of colloidal metal sulfides 6. Kinetics of interfacial reactions at ZnS-particles. Ber. Bunsen Ges. Phys. Chem. 88, 170–175.
Hernández-Gordillo, A., García-Mendoza, C., Alvarez-Lemus, M.A., Gómez, R., 2015. Photocatalytic reduction of Cr(VI) by using stacked ZnS layers of ZnS(en)x complex. J. Environ. Chem. Eng. 3, 3048–3054.
Hoque, M., Guzman, M., 2018. Photocatalytic activity: experimental features to report in heterogeneous photocatalysis. Materials 11, 1990.
Hu, X., Ji, H., Chang, F., Luo, Y., 2014. Simultaneous photocatalytic Cr(VI) reduction and 2,4,6-TCP oxidation over g-C_3N_4 under visible light irradiation. Catal. Today 224, 34–40.
Ito, A., Watanabe, T., Yada, S., Hamaura, T., Nakagami, H., Higashi, K., Moribe, K., Yamamoto, K., 2010. Prediction of recrystallization behavior of troglitazone/polyvinylpyrrolidone solid dispersion by solid-state NMR. Int. J. Pharm. 383, 18–23.
Jiang, Z., Sun, H., Qin, Z., Jiao, X., Chen, D., 2012. Synthesis of novel ZnS nanocages utilizing ZIF-8 polyhedral template. Chem. Commun. 48, 3620–3622.
Jin-Song, H., Ling-Ling, R., Yu-Guo, G., Han-Pu, L., An-Min, C., Li-Jun, W., Chun-Li, B., 2010. Mass production and high photocatalytic activity of ZnS nanoporous nanoparticles. Angew. Chem. 44, 1269–1273.
Jing, H., Guohua, C., Lo, I.M.C., 2005. Removal and recovery of Cr(VI) from wastewater by maghemite nanoparticles. Water Res. 39, 4528–4536.
Johne, P., Kisch, H., 1997. Photoreduction of carbon dioxide catalysed by free and supported zinc and cadmium sulphide powders. J. Photochem. Photobiol. A Chem. 111, 223–228.
Ju, L., Wu, P., Lai, X., Yang, S., Gong, B., Chen, M., Zhu, N., 2017. Synthesis and characterization of Fullerene modified ZnAlTi-LDO in photo-degradation of Bisphenol A under simulated visible light irradiation. Environ. Pollut. 228, 234–244.
Kaewanan, P., Sricharoen, P., Limchoowong, N., Sripakdee, T., Nuengmatcha, P., Chanthai, S., 2017. A fluorescence switching sensor based on graphene quantum dots decorated with Hg^{2+} and hydrolyzed thioacetamide for highly Ag^{+}-sensitive and selective detection. RSC Adv. 7, 48058–48067.
Kanemoto, M., Shiragami, T., Pac, C., Yanagida, S., 1992. Semiconductor photocatalysis. 13. Effective photoreduction of carbon dioxide catalyzed by zinc sulfide quantum crystallites with low density of surface defects. J. Phys. Chem. 96, 3521–3526.
Karthikeyan, T., Rajgopal, S., Miranda, L.R., 2005. Chromium(VI) adsorption from aqueous solution by Hevea Brasilinesis sawdust activated carbon. J. Hazard Mater. 124, 192–199.
Khalil, L.B., Mourad, W.E., Rophael, M.W., 1998. Photocatalytic reduction of environmental pollutant Cr(VI) over some semiconductors under UV/visible light illumination. Appl. Catal. B Environ. 17, 267–273.
Kongsricharoern, N., Polprasert, C., 1996. Chromium removal by a bipolar electrochemical precipitation process. Water Sci. Technol. 34, 109–116.
Konstantinou, I.K., Albanis, T.A., 2004. TiO-assisted photocatalytic degradation of azo dyes in aqueous solution: kinetic and mechanistic investigations: a review. Appl. Catal. B Environ. 49, 1–14.
Ku, Y., Jung, I.-L., 2001. Photocatalytic reduction of Cr(VI) in aqueous solutions by UV irradiation with the presence of titanium dioxide. Water Res. 35, 135–142.
Lan, M., Guo, R.-M., Dou, Y., Zhou, J., Zhou, A., Li, J.-R., 2017. Fabrication of porous Pt-doping heterojunctions by using bimetallic MOF template for photocatalytic hydrogen generation. Nano Energy 33, 238–246.
Lee, G.-J., Anandan, S., Masten, S.J., Wu, J.J., 2016. Photocatalytic hydrogen evolution from water splitting using Cu doped ZnS microspheres under visible light irradiation. Renew. Energy 89, 18–26.
Lee, P.-K., Chang, H.J., Yu, S., Chae, K.H., Bae, J.-H., Kang, M.-J., Chae, G., 2018. Characterization of Cr (VI) – containing solid phase particles in dry dust deposition in Daejeon, South Korea. Environ. Pollut. 243, 1637–1647.
Li, J.J., Wang, C.C., Fu, H.F., Cui, J.R., Xu, P., Guo, J., Li, J.R., 2017. High-performance adsorption and separation of anionic dyes in water using a chemically stable graphene-like metal–organic framework. Dalton Trans. 46, 10197–10201.
Li, P., Guo, M., Wang, Q., Li, Z., Wang, C., Chen, N., Wang, C.-C., Wan, C., Chen, S., 2019. Controllable synthesis of cerium zirconium oxide nanocomposites and their application for photocatalytic degradation of sulfonamides. Appl. Catal. B

Environ. 259, 118107.
Li, Y., Li, X., Yang, C., Li, Y., 2004. Ligand-controlling synthesis and ordered assembly of ZnS nanorods and nanodots. J. Phys. Chem. B 108, 16002–16011.
Liang, R., Jing, F., Shen, L., Qin, N., Wu, L., 2015a. MIL-53(Fe) as a highly efficient bifunctional photocatalyst for the simultaneous reduction of Cr(VI) and oxidation of dyes. J. Hazard Mater. 287, 364–372.
Liu, Q., Shen, J., Hua, T., Zhang, T., Yang, X., 2018. 3D Reduced graphene oxide aerogel-mediated Z-scheme photocatalytic system for highly efficient solar-driven water oxidation and removal of antibiotics. Appl. Catal. B Environ. 232, 562–573.
Liang, R., Shen, L., Jing, F., Wu, W., Qin, N., Lin, R., Wu, L., 2015b. NH_2-mediated indium metal–organic framework as a novel visible-light-driven photocatalyst for reduction of the aqueous Cr(VI). Appl. Catal. B Environ. 162, 245–251.
Liu, X., Pan, L., Zhao, Q., Lv, T., Zhu, G., Chen, T., Lu, T., Sun, Z., Sun, C., 2012. UV-assisted photocatalytic synthesis of ZnO–reduced graphene oxide composites with enhanced photocatalytic activity in reduction of Cr(VI). Chem. Eng. J. 183, 238–243.
Low, Z.-X., Yao, J., Liu, Q., He, M., Wang, Z., Suresh, A.K., Bellare, J., Wang, H., 2014a. Crystal transformation in zeolitic-imidazolate framework. Cryst. Growth Des. 14, 6589–6598.
Low, Z.X., Yao, J., Qi, L., Ming, H., Wang, Z., Suresh, A.K., Bellare, J., Wang, H., 2014b. Crystal transformation in zeolitic-imidazolate framework. Cryst. Growth Des. 14, 6589–6598.
Lu, W., Wang, W., Meng, S., Yin, W., Sun, S., Ling, Z., 2010. Enhanced photocatalytic hydrogen evolution under visible light over Cd_xZn_xS solid solution with cubic zinc blend phase. Int. J. Hydrogen Energy 35, 19–25.
Morris, W., Stevens, C.J., Taylor, R.E., Dybowski, C., Yaghi, O.M., Garcia-Garibay, M.A., 2012. NMR and X-ray study revealing the rigidity of zeolitic imidazolate frameworks. J. Phys. Chem. C 116, 13307–13312.
Murphy, C.J., Buriak, J.M., 2015. Best Practices for the Reporting of Colloidal Inorganic Nanomaterials. Chemistry of Materials 27, 4911–4913.
Niknam Shahrak, M., Ghahramaninezhad, M., Eydifarash, M., 2017. Zeolitic imidazolate framework-8 for efficient adsorption and removal of Cr(VI) ions from aqueous solution. Environ. Sci. Pollut. Control Ser. 24, 9624–9634.
Ouyang, S., Ye, J., 2011. β-AgAl1-xGaxO_2 solid-solution photocatalysts: continuous modulation of electronic structure toward high-performance visible-light photoactivity. J. Am. Chem. Soc. 133, 7757–7763.
Padhi, D.K., Parida, K., 2014. Facile fabrication of α-FeOOH nanorod/RGO composite: a robust photocatalyst for reduction of Cr(VI) under visible light irradiation. J. Mater. Chem. 2, 10300–10312.
Patterson, J.W., 1985. Industrial Wastewater Treatment Technology.
Qi-Long, Z., Qiang, X., 2014. Metal-organic framework composites. Chem. Soc. Rev. 43, 5468–5512.
Qiu, J., Zhang, X.F., Zhang, X., Feng, Y., Li, Y., Yang, L., Lu, H., Yao, J., 2018. Constructing $Cd_{0.5}Zn_{0.5}S$@ZIF-8 nanocomposites through self-assembly strategy to enhance Cr(VI) photocatalytic reduction. J. Hazard Mater. 349, 234–241.
Qu, J., Chen, D., Li, N., Xu, Q., Hua, L., He, J., Lu, J., 2017. Coral-inspired nanoscale design of porous SnS_2 for photocatalytic reduction and removal of aqueous Cr(VI). Appl. Catal. B Environ. 207, 404–411.
Rauf, M.A., Ashraf, S.S., 2009. Fundamental principles and application of heterogeneous photocatalytic degradation of dyes in solution. Chem. Eng. J. 151, 10–18.
Rengaraj, S., Venkataraj, S., Yeon, J.W., Kim, Y., Li, X.Z., Pang, G.K.H., 2007. Preparation, characterization and application of Nd–TiO_2 photocatalyst for the reduction of Cr(VI) under UV light illumination. Appl. Catal. B Environ. 77, 157–165.
Rieter, W.J., Pott, K.M., Taylor, K.M.L., Wenbin, L., 2008. Nanoscale coordination polymers for platinum-based anticancer drug delivery. J. Am. Chem. Soc. 130, 11584–11585.
Sabate, J., Anderson, M.A., Aguado, M.A., Giménez, J., Cervera-March, S., Hill, C.G., 1992. Comparison of TiO_2 powder suspensions and TiO_2 ceramic membranes supported on glass as photocatalytic systems in the reduction of chromium(VI). J. Mol. Catal. 71, 57–68.
Sadik, W.A., 2007. Effect of inorganic oxidants in photodecolourization of an azo dye. J. Photochem. Photobiol. A Chem. 191, 132–137.
Schrank, S.G., José, H.J., Moreira, R.F.P.M., 2002. Simultaneous photocatalytic Cr(VI) reduction and dye oxidation in a TiO_2 slurry reactor. J. Photochem. Photobiol. A Chem. 147, 71–76.
Selvi, K., Pattabhi, S., Kadirvelu, K., 2001. Removal of Cr(VI) from aqueous solution by adsorption onto activated carbon. Bioresour. Technol. 80, 87–89.
Seo, J.S., Whang, D., Lee, H., Jun, S.I., Oh, J., Jeon, Y.J., Kim, K., 2000. A homochiral metal-organic porous material for enantioselective separation and catalysis. Nature 404, 982–986.
Sethia, S., Squillante, E., 2004. Solid dispersion of carbamazepine in PVP K30 by conventional solvent evaporation and supercritical methods. Int. J. Pharm. 272, 1–10.
Shen, L., Liang, S., Wu, W., Liang, R., Wu, L., 2013. Multifunctional NH_2-mediated zirconium metal–organic framework as an efficient visible-light-driven photocatalyst for selective oxidation of alcohols and reduction of aqueous Cr(VI). Dalton Trans. 42, 13649–13657.
Shen, L., Luo, M., Liu, Y., Liang, R., Jing, F., Wu, L., 2015. Noble-metal-free MoS2 co-catalyst decorated UiO-66/CdS hybrids for efficient photocatalytic H_2 production. Appl. Catal. B Environ. 166–167, 445–453.
Shi, L.-n., Zhang, X., Chen, Z.-l., 2011. Removal of Chromium (VI) from wastewater using bentonite-supported nanoscale zero-valent iron. Water Res. 45, 886–892.
Spagnol, V., Sutter, E., Debiemme-Chouvy, C., Cachet, H., Baroux, B., 2009. EIS study of photo-induced modifications of nano-columnar TiO films. Electrochim. Acta 54, 1228–1232.
Su, H., Xie, Y., Xiong, Y., Gao, P., Qian, Y., 2001. Preparation and morphology control of rod-like nanocrystalline Tin sulfides via a simple ethanol thermal route. J. Solid State Chem. 161, 190–196.
Sun, B., Reddy, E.P., Smirniotis, P.G., 2005. Visible light Cr(VI) reduction and organic chemical oxidation by TiO_2 photocatalysis. Environ. Sci. Technol. 39, 6251–6259.
Tandra, G., Subhajit, B., Soumitra, K., De, S.K., 2009. ZnO nanowire arrays: synthesis, optical and field emission properties. J. Nanosci. Nanotechnol. 9, 5586.
Tartour, E., Zitvogel, L., 2013. Synthesis and enhanced Cr(VI) photoreduction property of formate anion containing graphitic carbon nitride. J. Phys. Chem. C 117, 4062–4068.
Velegraki, G., Miao, J., Drivas, C., Liu, B., Kennou, S., Armatas, G.S., 2018. Fabrication of 3D mesoporous networks of assembled CoO nanoparticles for efficient photocatalytic reduction of aqueous Cr(VI). Appl. Catal. B Environ. 221, 635–644.
Wang, C.C., Du, X.D., Li, J., Guo, X.X., Wang, P., Zhang, J., 2016a. Photocatalytic Cr(VI) reduction in metal-organic frameworks: a mini-review. Appl. Catal. B Environ. 193, 198–216.
Wang, C.C., Li, J.R., Lv, X.L., Zhang, Y.Q., Guo, G., 2014. Photocatalytic organic pollutants degradation in metal–organic frameworks. Energy Environ. Sci. 7, 2831–2867.
Wang, D., Jia, F., Wang, H., Chen, F., Fang, Y., Dong, W., Zeng, G., Li, X., Yang, Q., Yuan, X., 2018. Simultaneously efficient adsorption and photocatalytic degradation of tetracycline by Fe-based MOFs. J. Colloid Interface Sci. 519, 273–284.
Wang, J.C., Ren, J., Yao, H.C., Zhang, L., Wang, J.S., Zang, S.Q., Han, L.F., Li, Z.J., 2016b. Synergistic photocatalysis of Cr(VI) reduction and 4-Chlorophenol degradation over hydroxylated α-Fe_2O_3 under visible light irradiation. J. Hazard Mater. 311, 11–19.
Wang, F.X., Yi, X.H., Wang, C.C., Deng, J.G., 2017. Photocatalytic Cr(VI) reduction and organic-pollutant degradation in a stable 2D coordination polymer. Chin. J. Catal. 38, 2141–2149.
Wang, H., Qiao, X., Chen, J., Wang, X., Ding, S., 2005. Mechanisms of PVP in the preparation of silver nanoparticles. Mater. Chem. Phys. 94, 449–453.
Wang, H., Yuan, X., Wu, Y., Zeng, G., Chen, X., Leng, L., Wu, Z., Jiang, L., Li, H., 2015. Facile synthesis of amino-functionalized titanium metal-organic frameworks and their superior visible-light photocatalytic activity for Cr(VI) reduction. J. Hazard Mater. 286, 187–194.
Wang, K.H., Hsieh, Y.H., Wu, C.H., Chang, C.Y., 2000. The pH and anion effects on the heterogeneous photocatalytic degradation of o-methylbenzoic acid in TiO_2 aqueous suspension. Chemosphere 40, 389–394.
Wang, X., Liu, W., Fu, H., Yi, X.-H., Wang, P., Zhao, C., Wang, C.-C., Zheng, W., 2019. Simultaneous Cr(VI) reduction and Cr(III) removal of bifunctional MOF/Titanate nanotube composites. Environ. Pollut. 249, 502–511.
Wang, Y., Zhang, L., Liang, C., Wang, G., Peng, X., 2002. Catalytic growth and photoluminescence properties of semiconductor single-crystal ZnS nanowires. Chem. Phys. Lett. 357, 314–318.
Wee, L.H., Nikki, J., Sree, S.P., Christian, W., Elena, G., Fischer, R.A., Kirschhock, C.E.A., Martens, J.A., 2014. Local transformation of ZIF-8 powders and coatings into ZnO nanorods for photocatalytic application. Nanoscale 6, 2056–2060.
Xi, Z., Hanye, Z., Xiaofeng, W., Zhenyu, L., Longhua, G., Bin, Q., Guonan, C., 2013. Metal-organic framework (MOF): a novel sensing platform for biomolecules. Chem. Commun. 49, 1276.
Yanagida, S., Kawakami, H., Midori, Y., Kizumoto, H., Pac, C., Wada, Y., 1995. Semiconductor photocatalysis. ZnS-Nanocrystallite-Catalyzed photooxidation of organic compounds. Bull. Chem. Soc. Jpn. 68, 1811–1823.
Yi, X.-H., Ma, S.-Q., Du, X.-D., Zhao, C., Fu, H., Wang, P., Wang, C.-C., 2019a. The facile fabrication of 2D/3D Z-scheme g-C_3N_4/UiO-66 heterojunction with enhanced photocatalytic Cr(VI) reduction performance under white light. Chem. Eng. J. 375, 121944.
Yi, X.-H., Wang, F.-X., Du, X.-D., Wang, P., Wang, C.-C., 2019b. Facile fabrication of BUC-21/g-C_3N_4 composites and their enhanced photocatalytic Cr(VI) reduction performances under simulated sunlight. Appl. Organomet. Chem. 33, e4621.
Yin, R., Ling, L., Xiang, Y., Yang, Y., Bokare, A.D., Shang, C., 2018. Enhanced photocatalytic reduction of chromium (VI) by Cu-doped TiO_2 under UV-A irradiation. Separ. Purif. Technol. 190, 53–59.
Youn-Sang, B., Spokoyny, A.M., Farha, O.K., Snurr, R.Q., Hupp, J.T., Mirkin, C.A., 2010. Separation of gas mixtures using Co(II) carborane-based porous coordination polymers. Chem. Commun. 46, 3478–3480.
Yu, X., Yu, J., Cheng, B., Huang, B., 2009. One-pot template-free synthesis of monodisperse zinc sulfide hollow spheres and their photocatalytic properties. Chem. Eur J. 15, 6731–6739.
Zhang, F., Zhang, Y., Zhang, G., Yang, Z., Dionysiou, D.D., Zhu, A., 2018. Exceptional synergistic enhancement of the photocatalytic activity of SnS_2 by coupling with polyaniline and N-doped reduced graphene oxide. Appl. Catal. B Environ. 236, 53–63.
Zhang, L., Xia, W., Liu, X., Zhang, W., 2014. Synthesis of titanium cross-linked chitosan composite for efficient adsorption and detoxification of hexavalent chromium from water. J. Mater. Chem. 3, 331–340.
Zhang, X.V., Ellery, S.P., Friend, C.M., Holland, H.D., Michel, F.M., Schoonen, M.A.A., Martin, S.T., 2007. Photodriven reduction and oxidation reactions on colloidal semiconductor particles: implications for prebiotic synthesis. J. Photochem. Photobiol. A Chem. 185, 301–311.
Zhang, X.V., Martin, S.T., 2006. Driving parts of krebs cycle in reverse through

mineral photochemistry. J. Am. Chem. Soc. 128, 16032–16033.
Zhao, D., Sengupta, A.K., Stewart, L., 1998. Selective removal of Cr(VI) oxyanions with a new anion exchanger. Ind. Eng. Chem. Res. 37, 4383–4387.
Zheng, Y., Duan, F., Chen, M., Xie, Y., 2010. Synthetic $Bi_2O_2CO_3$ nanostructures: novel photocatalyst with controlled special surface exposed. J. Mol. Catal. A Chem. 317, 34–40.
Zhou, J., Dou, Y., Zhou, A., Guo, R.-M., Zhao, M.-J., Li, J.-R., 2017. MOF template-directed fabrication of hierarchically structured electrocatalysts for efficient oxygen evolution reaction. Adv Energy Mater 7, 1602643.
Zhou, R., Guzman, M.I., 2014. CO_2 reduction under periodic illumination of ZnS. J. Phys. Chem. C 118, 11649–11656.
Zhou, R., Guzman, M.I., 2016. Photocatalytic reduction of fumarate to succinate on ZnS mineral surfaces. J. Phys. Chem. C 120, 7349–7357.
Zou, J.-P., Wu, D.-D., Luo, J., Xing, Q.-J., Luo, X.-B., Dong, W.-H., Luo, S.-L., Du, H.-M., Suib, S.L., 2016. A strategy for one-pot conversion of organic pollutants into useful hydrocarbons through coupling photodegradation of MB with photoreduction of CO_2. ACS Catal. 6, 6861–6867.